Journal of Infrared, Millimeter, and Terahertz Waves
https://doi.org/10.1007/s10762-020-00717-y

Observation of Anomalously Strong Penetration of Terahertz Electric Field Through Terahertz-Opaque Gold Films Into a GaAs/AlGaAs Quantum Well

S. D. Ganichev[1] · S. N. Danilov[1] · M. Kronseder[1] · D. Schuh[1] · I. Gronwald[1] · D. Bougeard[1] · E. L. Ivchenko[2] · A. Ya. Shul'man[3]

Received: 16 February 2020 / Accepted: 1 June 2020 / Published online: 26 June 2020

Abstract

We observe an anomalously high electric field of terahertz (THz) radiation acting on a two-dimensional electron gas (2DEG) placed beneath a thin gold film, which, however, is supposed to be opaque at THz frequencies. We show that the anomalously strong penetration of the THz electric field through a very high conductive gold film emerges if two conditions are fulfilled simultaneously: (i) the film's thickness is less than the skin depth and (ii) the THz electric field is measured beneath the film at distances substantially smaller than the radiation wavelength. We demonstrate that under these conditions, the strength of the field acting on a 2DEG is almost the same as it would be in the absence of the gold film. The effect is detected for macroscopically homogeneous perforation-free gold films illuminated by THz laser radiation with a spot smaller than the film area. This eliminates the near field of the edge diffraction as a possible cause of the anomalous penetration. The microscopic origin of the effect remains unexplained in its details, yet. The observed effect can be used for the development of THz devices based on two-dimensional materials requiring robust highly conducting top gates placed at less than nanometer distance from the electron gas location.

Keywords Terahertz · Nanostructures · Thin metal films

✉ S. D. Ganichev
sergey.ganichev@physik.uni-regensburg.de

[1] Terahertz Center, University of Regensburg, 93040 Regensburg, Germany

[2] Ioffe Physico-Technical Institute, 194021 St. Petersburg, Russia

[3] Kotelnikov Institute of Radioengineering and Electronics RAS, 125009 Moscow, Russia

1 Introduction

It is hardly necessary to emphasize the importance of thin metal films in modern science and technology. Metal films with thickness ranging from a few Angstroms to tens of nanometers have received great attention in recent years. They are used in solar cells, detectors, electronic semiconductor devices, magnetic memory devices, optical coatings (such as anti-reflective coatings), chemical and biological sensors, plasmonic and terahertz devices, etc. Optical properties of thin metal films with thickness substantially smaller than the light wavelength λ are usually characterized by light reflectance and transmittance measured at distances much larger than λ, in the so-called far field (for review, see e.g. [1]).

These properties are rather well researched. Recently, an understanding of electromagnetic field characteristics at distances from metal films substantially smaller than the radiation wavelength has become increasingly significant. It is primarily caused by the development of near-field optics (see e.g. [2–9]). Furthermore, metal films are often used in the fabrication of metallic gates, metamaterials, plasmonic and near-field opto-electronic devices based on 2D materials (e.g., graphene, the most prominent example), topological insulators, and low-dimensional heterostructures. In these cases, the electric field distribution in the subwavelength vicinity of metal films plays a crucial role. It is known that the rough surface of a well-conducting metal film enhances the interaction of electromagnetic radiation with objects located near the film. The most famous example of this phenomenon in the visible band is the surface-enhanced Raman scattering (SERS) of light by organic molecules on the rough silver surface, when an increase takes place in the scattering cross section up to $10^5 - 10^6$ times presumably due to the plasma excitation in surface roughness features [10, 11]. In the terahertz band, a roughness of metal gate made of gold or aluminum film results in a nonlinear photoconductivity of a tunnel Schottky diode that corresponds to an increase in the local energy density of the electromagnetic field in some small regions of the gate relative to the energy density in the incident radiation up to $10^3 - 10^5$ times due to the field enhancement in the near zone during radiation diffraction by surface irregularities [12–15].

For homogeneous highly conductive films, however, it is expected that the radiation is totally reflected and the electric field behind the film should decrease by orders of magnitudes.

Here, we report on the observation of anomalously strong penetration of terahertz electric field through tens of nanometers thick homogeneous perforation-free gold films deposited on top of GaAs/AlGaAs heterostructures. Using the two-dimensional electron gas (2DEG) in GaAs quantum well as detector, we show that the electric field of THz radiation acting on the 2DEG located beneath the highly conductive gold film is almost the same as it would be without the gold film, given that two conditions are fulfilled simultaneously: (i) the gold film has a thickness d less than skin depth δ_s and (ii) the field is detected at a distance much less than the radiation wavelength λ. Taking into account the high conductivity σ of gold at terahertz frequencies [16–19], this is a very surprising result.

Indeed, it follows from classical electrodynamics that, under condition $\omega/\sigma \ll 1$, where ω is the angular frequency and σ is the conductivity, a metal film has a

reflection coefficient $|r| \leq 1$ and a transmission coefficient $|t| \ll 1$, even at thicknesses much thinner than the skin depth $\delta_s = c/\sqrt{2\pi\omega\sigma}$, where c is the speed of light. The dependence of metal film penetrability on the thickness d for the film placed on a dielectric substrate with the refractive index n_b is given under conditions of the classical skin effect by:

$$\frac{E_t}{E_i} = \frac{2\gamma t_0 \mathrm{e}^{-\beta d}}{(1-\mathrm{e}^{-2\beta d}) + \gamma(1+\mathrm{e}^{-2\beta d})} \,. \tag{1}$$

Here, E_t and E_i are complex amplitudes of the electric field in the transmitted and incident waves, $t_0 = 2/(1+n_b)$ is the amplitude transmission coefficient with no metal film:

$$\beta = \frac{1-i}{\delta_s} \,, \gamma = (1-\mathrm{i})\frac{1+n_b}{2}\sqrt{\frac{f}{\sigma}} = (1-\mathrm{i})(1+n_b)\pi\frac{\delta_s}{\lambda} \,,$$

$f = \omega/2\pi$ is the frequency, and λ is the wavelength.

Considering this equation for thin films characterized by $2|\beta|d \ll 1$, we obtain in accordance with the impedance expression provided by Tinkham [20, 21]:

$$t = \frac{E_t}{E_i} \cong \frac{t_0}{1+d\frac{\beta}{\gamma}} = \frac{t_0}{1+\frac{\lambda}{(1+n_b)\pi\delta_s}\frac{d}{\delta_s}} = \frac{t_0}{1+\frac{4\pi d\sigma}{c(1+n_b)}} \,. \tag{2}$$

From here follows that in order to achieve a radiation transmission through the film close to unity, the film thickness d needs to be several orders of magnitude smaller than the skin depth δ_s, so that $d/\delta_s \ll (1+n_b)\pi\delta_s/\lambda$. Accordingly, for the wavelength of about $\lambda \approx 100\ \mu$m (frequency $f \approx 3$ THz), an almost unchanged electric field amplitude is only expected for the gold film thickness $d < 1$ Å. Consequently, the electric field at the second boundary as well as the amplitude of the transmitted electromagnetic wave at any real film thickness should be much less than the field amplitude in the incident wave. Noteworthy, that this abrupt decrease in the amplitude of the electric field inside the metal occurs immediately at the vacuum-metal interface, where the electric fields of the incident and reflected waves are almost mutually canceled due to the high electrical conductivity of the metal. A further decrease in the field amplitude deep into the metal is characterized by the parameter δ_s and is of little significance under our conditions $d < \delta_s$. A. E. Kaplan has made recently analogue conclusions by using also the impedance language [22]. Figure 1 shows the transmitted electric field amplitude, which has been calculated after Fresnel formulae as a function of the gold film thickness for three different frequencies used in our experiments (for calculation details see Appendix 1).

It demonstrates that for films with a thickness of 10 nm or more, the field magnitude should decrease by at least two orders of magnitude. This has been observed in a number of experiments on far-field transmission of THz radiation (see e.g. Ref. [16]). It was also detected in our reference experiments performed under conditions $d_i \gg \lambda$ and/or $d > \delta_s$, where d_i is the distance from the film to the QW position at which the field is probed. The unchanged electric field amplitude, observed in our experiments for $d_i \ll \lambda$ and $d < \delta_s$, discloses an obvious contradiction to fundamental textbook arguments given above. While the origin of this phenomenon is unexplained in its microscopic details yet, we believe that our experiments presented below may serve

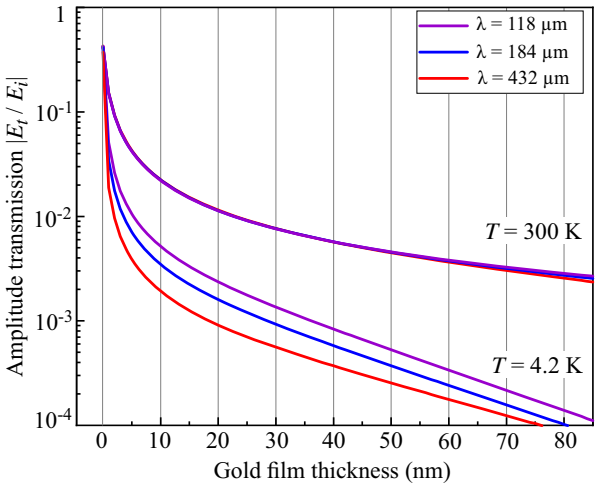

Fig. 1 Ratio of transmitted and incident radiation electric fields as a function of the gold film thickness. Data are presented for three wavelengths and two temperatures

as basis for an understanding of a fundamental physical problem providing insight into a structure of electromagnetic fields at the metallic film-semiconductor interface.

The paper is organized as follows. In Section 2, we briefly discuss the essential features of our research methodology and the properties of the gold-film/semiconductor structures under study. The results on THz field penetrability are presented in Section 3. The last section summarizes the work. We also supply our paper by Appendixes 1–3 presenting description of the equations used for calculations of curves in Fig. 1, experimental methods, and additional details of growth and electric characteristics of the gold films.

2 Experimental Technique and Samples

Gold films are deposited on top of GaAs/AlGaAs heterostructures leaving either half of the sample uncovered or depositing gold only on a predefined rectangle (see Figs. 2a and 3). The anomalous penetrability of Au films has been observed by detecting the photoconductivity [14] or the linear photogalvanic effect (LPGE) [14, 23] excited by THz radiation in a GaAs/AlGaAs quantum well (QW) placed underneath the gold film at a distance d_i much smaller than the radiation wavelength λ in the GaAs ($d_i \ll \lambda$). These effects yield photosignals with an amplitude proportional to the second power of the radiation electric field acting on the 2D electron gas in the QW (for details, see Appendix 2). We compared the photosignals obtained for light illuminating either gold-covered or gold-uncovered areas of the sample. Taking the ratio of these signals $\tilde{R}$, we obtain the reduction of the radiation intensity caused by the gold film. The experimental geometry is shown in Fig. 2a. In particular, the beam having the spot size (diameter about 1.5 mm, see Appendix 2)

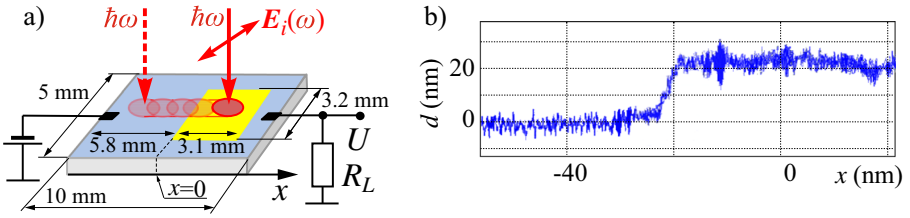

Fig. 2 **a** Experimental setup. *Vertical downward arrows* and *red spots* illustrate the polarized THz radiation beam scanned across the sample. The beam was scanned following the middle line along the long side of the sample. Steps of 100, 200, or 250 μm were used. The geometrical sizes, being of the same order for all samples, and typical gold film profile are exemplary shown for sample #B-20E. **b** Thickness profile $d(x)$ of 20-nm-thick evaporated gold film measured by DektakXT Stylus Profiler (Bruker GmbH). Zero thickness d corresponds to the surface of GaAs top cap layer

smaller than the gold film area (about 3.5×3.5 mm^2) was scanned across the sample. Linearly polarized laser radiation was applied at normal incidence. Illuminating the sample changes the conductivity of the QW, which for biased sample resulted in a voltage drop across the load resistance R_L. In some samples, it also yielded a photovoltage caused by the linear photogalvanic effect. The signal in response to the modulated radiation was registered by a standard lock-in technique. Experiments were carried out applying continuous wave cw THz molecular laser operating at wavelengths of 118, 184, or 432 μm [24, 25]. Corresponding frequencies (photon energies) are $f = 2.54$ THz ($\hbar\omega = 10.51$ meV), $f = 1.62$ THz ($\hbar\omega = 6.7$ meV), and $f = 0.69$ THz ($\hbar\omega = 2.87$ meV). Experiments were performed at room and liquid helium temperatures. More details are given in Appendix 2.

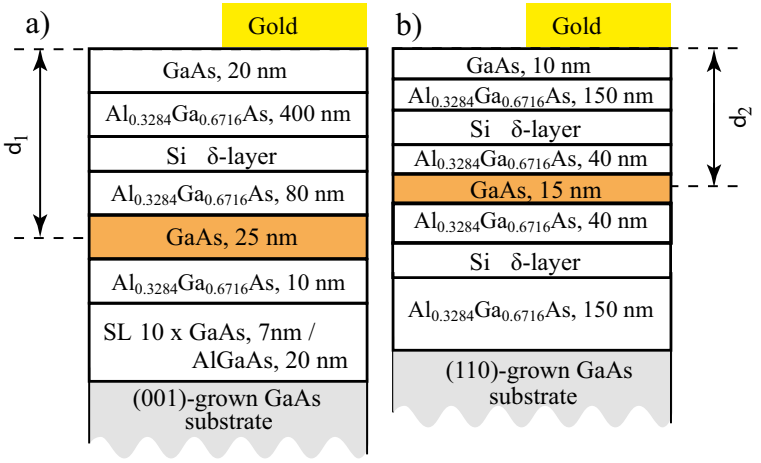

Fig. 3 Structure cross-section of wafers type #A, panel (**a**), and #B, panel (**b**), used for fabrication of samples. Single GaAs QW is grown at a distance d_i from the top cap layer surface. Structures are grown on 350-μm-thick GaAs substrate

Two groups of molecular beam epitaxially (MBE) grown GaAs/GaAlAs heterostructures with single GaAs quantum well were used. Figure 3 shows a cross-section of the structure. Four wafers of the same heterostructure design, grown on (001)-oriented GaAs substrate and hosting a 25-nm-thick QW, were used for fabrication of type #A samples. Wafer #B, grown on a (110)-oriented GaAs substrate and hosting a 15-nm-thick QW, was used for fabrication of samples of type #B. The latter structure, with a reduced point group symmetry compared with (001)-grown structures, allows us to measure besides the photoconductivity also the photogalvanic effect excited by normal incident THz radiation [26] in unbiased samples (for details, see Appendix 2). Substrates are made of 350-μm-thick semi-insulating GaAs and are transparent for THz radiation. The density and mobility of electrons in 2DEG, obtained by magnetotransport experiments performed at $T = 4.2$ K, are $n \approx 10^{11}$ cm^{-2} and mobility $\mu \approx 10^6$ cm^2/V $\cdot$ s, respectively.

Gold films with thicknesses 10, 20, and 85 nm were fabricated either by MBE directly connected to the GaAs-MBE or thermal vacuum evaporation. For the latter, the samples were exposed to air before the Au deposition. The 3.5×3.5 mm^2 gold films covered about half of the sample surface with a rectangular shape with about 5 mm width and 10 mm length. The shape and position of the gold layer are shown in Fig. 2a. For optoelectronic measurements, after the gold film deposition, a pair of ohmic contacts was prepared in the middle of short edges (see Fig. 2a).

MBE-grown gold films were used for preparation of samples made from wafers #A1, #A2, and #A4. For that subsequently to the semiconductor growth, the wafers were transferred in situ from the III-V to the metal/oxide MBE where the Au layers were grown on parts of the 2-in. wafer by a movable shadow mask between the sample and the Knudsen cell. Reflection high-energy electron diffraction (RHEED) was used to check the crystalline quality of the layer, and to crosscheck the growth rate by RHEED oscillations. In the following, these samples will be labeled as e.g. sample #A1-20M, which shows that the sample is fabricated from the wafer #A1, has a 20-nm-thick film deposited on top of the heterostructure cap layer (the number after hyphen), and it is grown by MBE (last letter). More details are given in Appendix 3A.

Thermal vacuum evaporation was used for preparation of samples made from wafers #A1, #A3, and #B. Gold films were deposited on an unheated wafer using a Leybold Univex system. The thickness of the film was monitored by a quartz-microbalance. The samples were not annealed after deposition. A metallic shadow mask was used to cover only half of the sample. The gold structure size was chosen such that all sample edges are not covered to avoid short-cutting the QWs (see Fig. 2a). These samples are labeled in the same way as MBE samples, e.g., sample #B-20E, but with last letter E in the notation, indicating that the film is made by vacuum evaporation. For some measurements aimed to study the gold penetrability for the distances of gold film to QW larger than the radiation wavelength ($d_i \gg \lambda$), we prepared sample with 20-nm gold film deposited on the backside of the sample's substrate instead of the deposition onto the top layer. This fact is reflected in the sample label by an additional letter "S," i.e., sample #A3-20ES.

Figure 4 shows typical atomic force microscopy (AFM) images of the fabricated gold films. These data show that the thickness fluctuations in MBE-grown films do not exceed 20% and in evaporated films is less than 25%. Consequently, the AFM

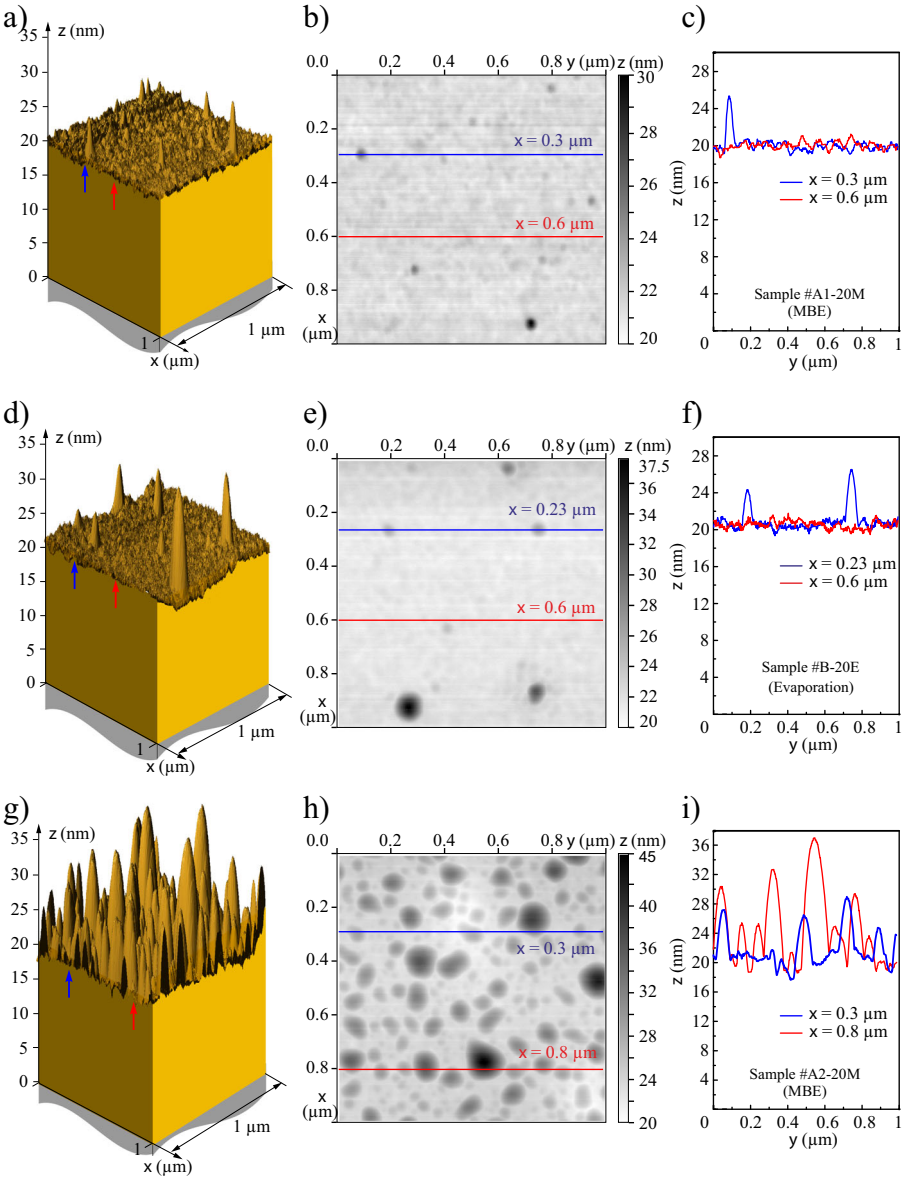

Fig. 4 AFM profile of 20-nm gold layers measured for different samples. Images obtained on samples: **a**–**c** sample #A1-20M (MBE grown gold); **d**–**f** sample #B-20E (evaporated gold); and **g**–**i** sample #A2-20M (MBE grown gold)

images ensure that there are no perforations of film at least up to the resolution limit of the AFM. Figure 4g–i show AFM image of sample #A2-20M. While being grown by MBE, due to unknown reason, this sample is characterized by large thickness

fluctuations (at some points up to 80%). We included this sample in the study in order to check how important the surface roughness is for the gold film penetrability.

Besides the AFM measurements, yielding gold film profiles on a micrometer scale, we checked the film thickness over the whole sample length. The results are shown in Fig. 2b. Here, the layer thickness was measured by DektakXT Stylus Profiler (Bruker GmbH). This is a contacting method using low-force low-inertia scanning needle and has an accuracy of 4 Ångström. The data show that the thickness variation is near ± 5 nm and the border of the gold film is rather sharp ($\Delta x \simeq 10 \div 15 \mu$m).

3 Results

3.1 Room Temperature Data

Applying normally incident linearly polarized cw radiation we detect an increasing resistivity of the QW's in all samples upon illumination (negative photoconductivity). The change of the QW's conductivity is caused by the electron gas heating due to Drude-like free carrier absorption and consequent change of the electron mobility (so-called hot electron bolometer or μ-photoconductivity effect). The signal strength is proportional to the square of the amplitude of the electric field acting on the 2DEG. The negative sign of the photoconductivity is due to the fact that at room temperature the mobility is governed by phonon scattering, which becomes more efficient upon heating. This phenomenon is well known and deeply studied for various bulk and low dimensional materials including GaAs QWs with characteristics similar to that used in our work, more details are given in Appendix 2. Thus, detailed discussion of the physical mechanisms of the photo-response is out of scope of the present paper aimed to anomalous penetrability observed in gold films.

Figure 5a and b show the main result of the work obtained for 20 and 10 nm thick gold films deposited on the top surface. Moving the beam across the surface from the area without gold film to that covered by gold, surprisingly the photoconductive signal does not change much. It remains almost the same even if the spot is located fully within the gold film area! This anomalous penetrability was observed for films fabricated by both methods and having different surface roughness. We emphasize that the data are obtained for gold thicknesses at which according to Fresnel formulae the amplitude of the electric field penetrating through the film should be decreased by orders of magnitude (see Fig. 1 and Section 1). A possible reason for this result could be film perforations or percolation effects. The latter was studied in detail by the transmission measurements of gold films of various thicknesses [16]. It demonstrated that while radiation transmission is substantially enhanced for film with thickness up to 7 nm, the percolation effects for 20-nm-thick film become absent. AFM images discussed above demonstrate that there are no perforations of film at least up to the resolution limit of the AFM. This makes near-field diffraction effect as a possible reason of the electric field enhancement very unlikely. We also note that the results for samples #A1-20M with the most homogeneous gold film, (see Fig. 4a–c) and #A2-20M with the most rough film surface (see Fig. 4g–i) are almost the same. Would the effect be caused by the film-surface roughness or near-field diffraction, we would

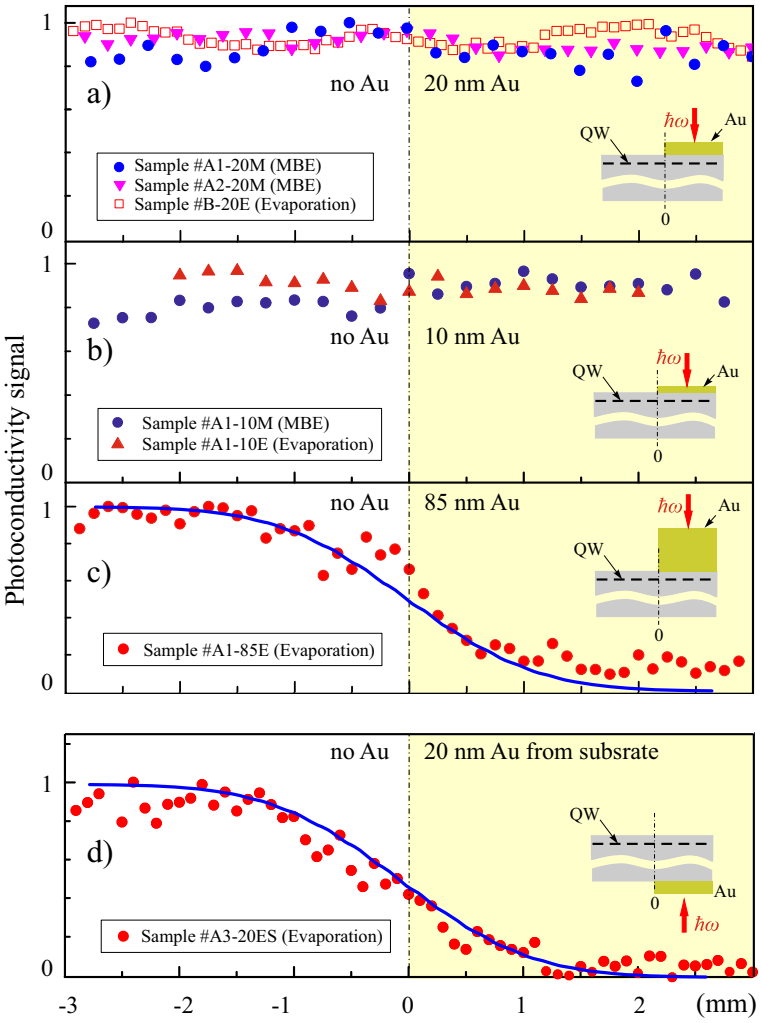

Fig. 5 Coordinate dependence of the normalized photoconductivity signal in response to *cw* radiation with $\lambda = 118$ μm obtained in samples with gold film of thickness; **a** 20 nm, **b** 10 nm, **c** 85 nm, and **d** 20 nm. For three first panels, (**a**)–(**c**) gold films were fabricated on top of the heterostructure. In these cases, normally incident THz laser radiation was applied from the top side. In the last panel, (**d**) gold film was deposited on the substrate side and normally incident radiation was applied from the substrate side. Note that semi-insulating GaAs substrates are transparent for THz radiation. The data are normalized on the signal for the area without gold film. The laser beam was scanned along the axis x. The areas covered by gold are marked by a yellow background. Solid lines in panels (**c**) and (**d**) show calculated integral intensity of a Gaussian beam scanned across the opaque film. Parameters of the Gaussian beam have been obtained applying pyroelectric camera; see Appendix 2

expect to detect differences in the electric field penetration in these samples with essentially different gold surface profiles.

To justify that our weak laser radiation does not modify the gold film surface, e.g., drills holes in the films, we first took an AFM image at a marked position,

then exposed the sample to the radiation for a long time (35 min), and finally again obtained the AFM image at a previously marked position. For that, we applied radiation with power levels even higher (115 mW) than those used for photoconductive measurements (40 mW). The results shown in Fig. 6 demonstrate that the exposure with cw laser radiation does not change the gold thickness and the surface roughness, excluding laser radiation-induced gold ablation in our experiments.

In the measurements discussed above, two conditions have been simultaneously fulfilled: (i) film thickness d was less than the skin depth δ_s (for used frequency about 65 nm at room temperature; see Appendix 3B), and (ii) the distance to QW-based detector, d_i, was much smaller than the wavelength λ in GaAs.

Furthermore, violation of any of these conditions results in a drastic reduction of the photoconductive signal demonstrating that the film becomes opaque. Figure 5c shows the results obtained for a 85-nm gold film which is thicker than the skin depth. Scanning the beam from uncovered parts to gold-covered parts results in the substantial signal reduction. The data can be well fitted by a curve describing the intensity reduction expected for a Gaussian beam moving across the boundary of an opaque material (see curve in Fig. 5c). The Gaussian beam parameters used for the calculation were determined applying a pyroelectric camera (corresponding image and discussion are presented in Appendix 2).

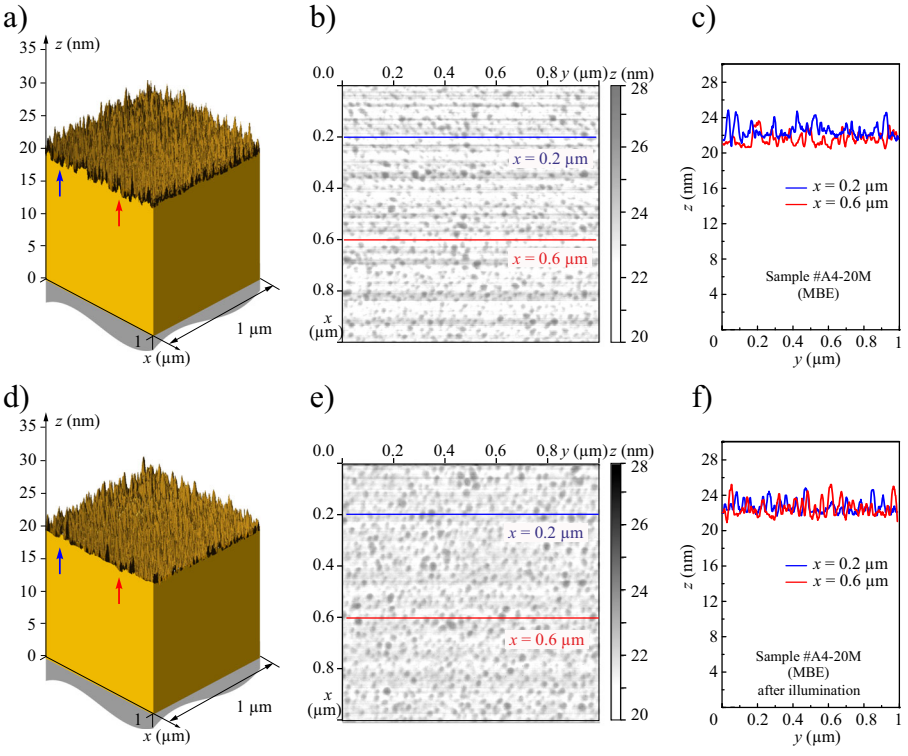

Fig. 6 AFM profile of 20 nm MBE grown gold film (Sample #A4-20M). Panels **a**–**c**, before illumination; and **d**–**f**, after 35-min exposition to cw-laser radiation power $P \approx 115$ mW ($\lambda = 118\ \mu$m)

Placing a detector at a distance $d \geqq \lambda$ and, consequently, measuring the far-field transmission through films we confirm that, as expected from Fresnel formulae, our 20-nm films are opaque for THz radiation. This has been verified by two methods. In the first one, we deposited gold film on the bottom side of the heterostructure and illuminated the film from the substrate side (see inset in Fig. 5d). In this case, the distance between the gold film and QW detector (of the order of 350 μm) becomes larger than the radiation wavelength 118 μm. Note that the latter is additionally reduced in GaAs by a refractive index of about 3.5. Figure 5d shows the result for 20-nm-thick gold film deposited on the backside of the substrate, sample #A3-20ES. It demonstrates that the photoconductive signal drastically reduces by shifting the beam to the gold film and the scan can be well fitted by intensity reduction at movement of the Gaussian beam across an opaque film. In the second method, we measured the the radiation transmission of a film for samples with 20-nm gold film placed on top of the heterostructure. Now, however, instead of measuring photoconductive signal, we measured a signal of a large area with a pyroelectric detector placed behind the sample at a distance os several millimeters, i.e., much larger than λ (see Fig. 7). The scans are shown in Fig. 7 and demonstrate that the signal and, correspondently, radiation transmission become zero for a laser spot located within the gold-film area of samples.

In all measurements described above, the gold film penetrability was studied by comparing photoconductive signals obtained for radiation illuminating the gold-film-free and gold-film-coated areas of samples. It is noteworthy that the same result was achieved by using a completely different effect—photogalvanic current excited in QWs by terahertz radiation. To obtain a significant signal, in these experiments, we used radiation of pulsed THz laser yielding single 100-ns pulses (see Appendix 2). The polarization dependencies of the photocurrent generated by pulsed THz radiation in unbiased sample #B for radiation spot positions at gold-film-free sample area and within the 20-nm gold film–coated area are shown in Fig. 8a and b, respectively. The data reveal that the magnitude of the signal and its polarization dependence

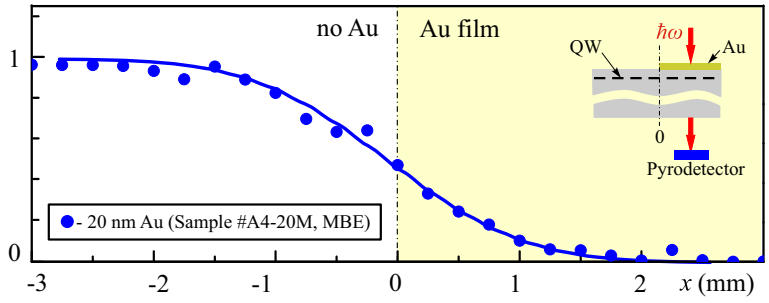

Fig. 7 Coordinate dependence of the radiation transmission measured by pyroelectric photodetector placed directly after the sample #A4-20M with 20 nm (*blue circles*) gold film grown by MBE. The data are normalized on the signal for the area without gold film. Note that semi-insulating GaAs substrates are transparent for THz radiation. The data are obtained applying for *cw* laser radiation with λ118 μm. *Solid lines* show calculated integral intensity of a Gaussian beam scanned across the opaque film. Parameters of the Gaussian beam have been obtained applying pyroelectric camera; see Appendix 2

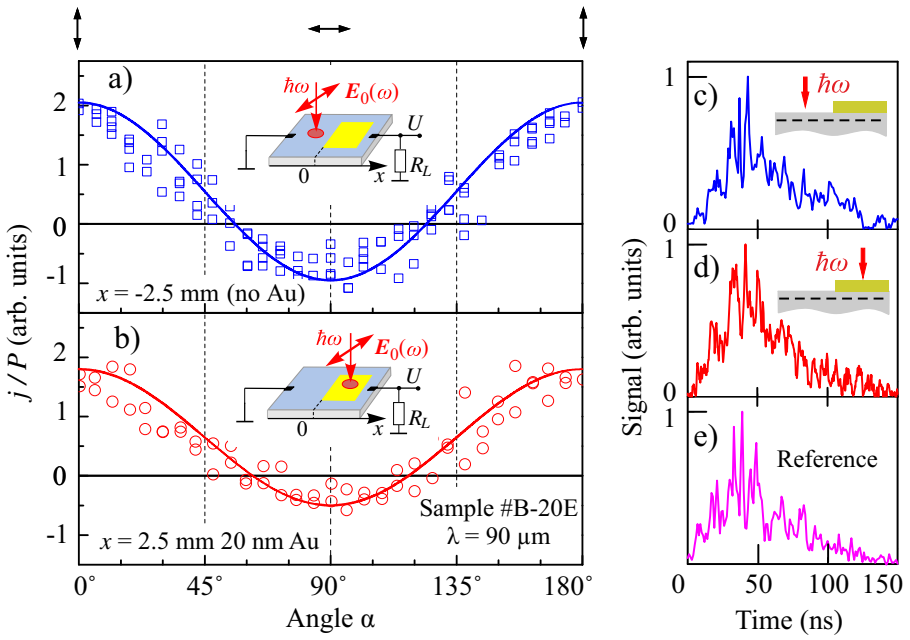

Fig. 8 **a**, **b** Photocurrent as a function of the azimuthal angle α measured in sample #B-20E. Data are taken for irradiation of gold-film-free part (**a**) of the sample (*blue points*) and gold-film-covered part (**b**) (*red points*, film thickness 20 nm). Data are obtained with radiation of pulsed laser operating at wavelength $\lambda = 90$ μm. The total pulse duration about 100 ns and peak pulse power $P \approx 800$ W. *Solid lines* are fits by phenomenological equation (10) of Appendix 2 describing LPGE and given by $j/P = \chi_- + \chi_+ \cos 2\alpha$. Panel **c**–**e** show pulse traces that show photosignal for irradiation of gold-film-free-part (**c**), gold-film-covered part (**d**) of the sample and response of the reference photon drag detector (**e**)

are almost the same for both spot positions. This result is in accordance with the photoconductivity data obtained on the same sample (see Fig. 5a). Essentially, new information obtained by LPGE is that not only the radiation electric field magnitude acting on 2D electrons but also its polarization remains the same. Polarization dependence of the photocurrent is described by $j/P = \chi_- + \chi_+ \cos 2\alpha$, being in agreement with the phenomenological theory of the LPGE (see Eq. 10 in Appendix 2). The polarization dependence for the conditions relevant to our experiment, i.e., normal incidence excitation of (110)-oriented GaAs/AlGaAs QWs and the current measured along [110]-direction is discussed in Appendix 2 (see Eq. 10). The mechanisms of the LPGE in such QWs involve asymmetric scattering of photoexcited electrons; they are well known and will not be discussed here (for somewhat more details see Appendix 2).

To measure rather weak LPGE currents, we applied pulsed laser radiation with possibly low intensity allowing us to avoid radiation-induced gold film destruction. Using short radiation pulses additionally allowed us to analyze the time constant of the photoresponse. Characteristic pulse traces, shown in Fig. 8c–e, demonstrate that the photoresponse for both spot positions reproduces short spikes caused by the spontaneous mode-locking (time constant less than 10 ns). Note that the same time

constants were obtained for photoconductive signals measured for illumination of areas without and with gold film (not shown). These short response times are in agreement with characteristics times of both of LPGE and μ-photoconductivity (see Appendix 2). The time scale as well as the coincidence of the time responses for the illumination of gold-film-free and and gold-film-coated sample parts additionally confirms that in both geometries the origin of the photosignals is identical.

3.2 Low-Temperature Measurements

Anomalous penetrability of terahertz electric fields through 20-nm gold films deposited on a GaAs quantum well structure was also observed at liquid helium temperatures. For these measurements, the sample was placed in an optical cryostat with z-cut crystal quartz windows. The photoconductive signal excited by normally incident radiation was measured as a function of an external magnetic field applied perpendicularly to the film. The data were obtained for three radiation wavelengths 118, 184, and 432 μm corresponding to frequencies 2.54, 1.68, and 0.69 THz, respectively. We measured photoconductive signal for two sample positions at which radiation was focused on gold-film-covered or gold-film-free parts of the sample (see Fig. 9). The values of the ratio $\tilde{R}$ were calculated as a ratio of these signals. The inset in Fig. 9 shows the frequency dependence of the intensity reduction obtained for zero magnetic field. In contrast to the room temperature data yielding for 20-nm-thick film $\tilde{R} \approx 1$ (see the inset in Fig. 9), at low temperature $\tilde{R}$ varies from ≈0.6

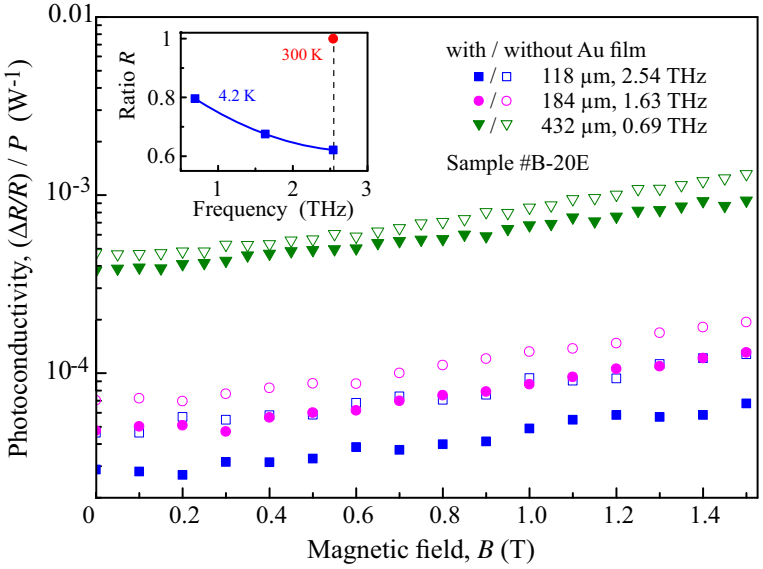

Fig. 9 Magnetic field dependence of the photoconductive signal obtained for two spot positions with radiation focused on sample areas without and with 20 nm gold film. The data are obtained at liquid helium temperature. *Inset* shows frequency dependence of the ratio $\tilde{R}$ of the signals obtained at zero magnetic field for illumination of gold-film-covered and gold-film-free area of the sample

to 0.8 by frequency decrease from 2.54 to 0.69 THz. Note that signals for both spot positions behave equally upon magnetic field variation showing that the signals are caused by the same mechanism. The observed increase of the photoconductive signal with increase of magnetic field is attributed to magnetic field-induced modification of scattering mechanisms and its discussion is beyond the scope of the present paper. We also note that, besides the drastically larger electric field compared with that expected from Fresnel formulas, the field reduction is characterized by frequency dependence opposite to that of the far-field gold film transmission (see Fig. 1).

The observed temperature and frequency behavior of the ratio $\tilde{R}$ qualitatively correspond to that of the skin depth. Being aware that it can not be directly applied to our case since the electron mean-free path is larger than the gold film thickness d we, nevertheless, like to pay attention to these similarities. The skin depth δ_s can be re-written as:

$$\delta_{\mathrm{s}} = \sqrt{\frac{\rho}{\pi f \mu_0}}. \tag{3}$$

Due to the reduction of the film resistivity upon temperature decrease (see Appendix 3B), the skin depth at low temperatures is reduced compared with that at room temperature. Furthermore, the skin depth depends on frequency as $\sqrt{1/f}$, i.e., becomes smaller for higher frequencies. In 20-nm-thick gold films at room temperature, the skin depth, being of the order of 65 nm for $f = 2.54$ THz (see Appendix 3B), is about three times larger than the film thickness. At 4.2 K, however, these values become comparable. Consequently, cooling the sample results in partial violation of the inequality $\delta_{\mathrm{s}} > d$, which was shown above to be crucial for the anomalous penetrability. Both tendencies, the decrease of the ratio $\tilde{R}$ with the temperature decrease at constant frequency or with frequency increase at constant temperature, are detected in our experiments (see inset in Fig. 9).

4 Summary

To summarize, we observe an anomalously strong penetration of THz radiation electric fields through almost homogeneous, perforation-free gold films deposited on semiconductor heterostructures with a conductive quantum well placed beneath the film at a distance substantially smaller than the radiation wavelength. We detected no field amplitude reduction as long as two conditions are simultaneously fulfilled: (i) the thickness of a highly conductive film is less than the skin depth (about 65 nm at room temperature and for the frequencies used in the study) and (ii) the distance to the QW-based detector is much smaller than the wavelength. Our measurements demonstrate that a violation of any of these conditions results in a drastic reduction of the photosignal, showing that the film becomes opaque. In this case, the result is described by the Fresnel formula. So far, we have no microscopic picture for this striking result. We note that, while we did our best to reduce the surface roughness, we cannot exclude completely inhomogeneities of the metal film, particularly on its internal surface, which would result in the effective conductivity to be less than expected by general frequency scaling law of DC bulk conductivity of the material. While focusing only on THz/gold/AlGaAs, we bear in mind that the effect should

be also present in other systems as far as as the two abovementioned conditions are fulfilled simultaneously. At terahertz frequencies, these conditions can be satisfied for various metals with high enough values of high-frequency conductivity, such as gold, silver, and aluminum. For higher frequencies, i.e., in near infrared and visible range, the conductivity decreases, and metals become less reflective, so that the field can penetrate through metal films of feasible thicknesses. As concerning the AlGaAs QWs used in our experiments, the only aim of it is a technical realization of local radiation electric field detection at nanometer scale distances from the metal film surface. Electrical photoresponse to terahertz radiation has been observed in a great number of low-dimensional systems, different QWs and heterostructures, graphene, 2D materials etc., which offer a number of ways to realize such experiments. The observed effect seems attractive for the development of THz devices based on 2D materials, which usually require robust top gates made of highly conductive metal films usually placed at less than 1 nm distance from the electron gas location.

Appendix 1: Transmission Through Au Film

The data plotted in Fig. 1 are obtained from Fresnel formulae. The amplitude transmission coefficient through the system "vacuum (0) – Au film (1) – semi-infinite substrate (2)" is given by [27]:

$$t = \frac{t_{10}t_{21}e^{i\phi}}{1 - r_{01}r_{21}e^{2i\phi}}, \qquad \phi = 2\pi\sqrt{\varepsilon_1}\frac{d}{\lambda}. \tag{4}$$

Here, d and ε_1 are the thickness and the dielectric function of the Au film, $r_{ij} = -r_{ji}$ and t_{ij} are the amplitude coefficients for reflection and transmission of the light falling from a half-infinite medium i ($i = 0$ in vacuum and $i = 1$ in layer 1) on the half-infinite medium j, given by the Fresnel formulae for normal incidence:

$$t_{10} = \frac{2}{1+n_1}, \; t_{21} = \frac{2n_1}{n_1+n_b}, \; r_{01} = \frac{n_1-1}{n_1+1}, \; r_{21} = \frac{n_1-n_b}{n_1+_b}, \tag{5}$$

where we introduced $n_1 = \sqrt{\varepsilon_1}$ and the refraction index of the substrate $n_b = \sqrt{\varepsilon_b}$.

For a metallic plate, we have the dielectric function in the following form:

$$\varepsilon_1 = 1 - \frac{\omega_p^2}{\omega(\omega + i/\tau)}. \tag{6}$$

For gold $\hbar\omega_p = 8.5$ eV, and momentum relaxation time in metal $\tau = 14$ fs [28] at room temperature, and $\tau = 238$ fs at liquid helium temperature [29]. For the substrate, we take the dielectric function of GaAs, $\varepsilon_b = 13$.

Appendix 2: Radiation Sources and Experimental Details

Experiments were carried out applying continuous wave cw THz molecular laser [24, 25] operating at wavelengths of 118, 184, or 432 μm. Corresponding frequencies (photon energies) are $f = 2.54$ THz ($\hbar\omega = 10.51$ meV) and $f = 1.62$ THz

($\hbar\omega = 6.7$ meV), and $f = 0.69$ THz ($\hbar\omega = 2.87$ meV). These single laser lines were obtained with methanol and difluoromethane as active media. The radiation power on samples was about 40 mW. The radiation was modulated by a chopper at a frequency of $f \approx 130$ Hz. The beam cross-section had the Gaussian shape which was monitored by a pyroelectric camera [30]. The spot sizes at the full width at half maximum (FWHM) are 1.5 mm for $\lambda = 118$ μm, 2 mm for $\lambda = 184$ μm, and 3 mm for $\lambda = 432$ μm. Image for radiation with $\lambda = 118$ μm is shown in Fig. 10a. They are smaller than the size of the 5×5 mm^2 square-shaped gold film. To control the incidence power of the laser terahertz radiation, a pyroelectric detector was used. In an additional experiment, aimed to measure kinetic of the photoconductive signal, we also used a pulsed NH_3 laser [31, 32], operating at $\lambda = 90.5$ µm ($f = 3.31$ THz, $\hbar\omega = 13.70$ meV). The laser was optically pumped by transversely excited atmospheric pressure (TEA) CO_2 laser [33, 34]. Single pulses with a duration of the order of 100 ns and peak power about several kilowatts were used. To control the incidence power of the lasers, the photon drag detector [35] was used. An example of the beam cross-section obtained with the pyroelectric camera is shown in Fig. 10b. The spot has a smaller size than gold films. The photoconductivity setup differs from that used for cw by the value of the load resistance $R_L = 50$ Ω only. The photovoltage across the load resistance was detected by a digital oscilloscope. In experiments on LPGE, we controlled and rotated the polarization plane of linearly polarized radiation by the azimuth α. For that, we used crystal quartz lambda-half plate. Note that for $\alpha = 0$ radiation is polarized along the y-direction.

To conclude on the gold film penetrability, we compared amplitudes of photoconductive or photovoltage signals obtained for illumination of gold film with that caused by illuminating of the gold-film-free area (see Fig. 2a).

Irradiation of QWs results in a free carrier (Drude-like) absorption of THz radiation resulting in electron gas heating. An increase of the electron temperature T_e changes the electron mobility μ which can be detected as a photoconductive signal.

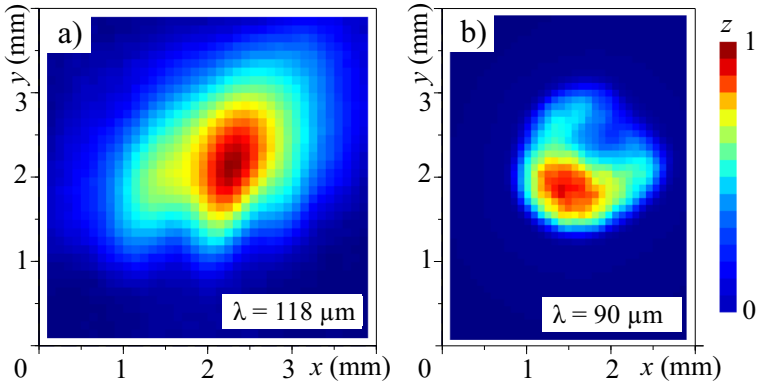

Fig. 10 Beam profiles of **a** cw laser operating at $\lambda = 118$ μm with the weighted mean beam diameter of 1.68 mm; **b** pulsed laser operating at $\lambda = 90$ μm with weighted mean beam diameter of 1.29 mm

If heating is weak, the radiation-induced variation of the conductivity $\Delta\sigma$ can be well approximated by the simple expression [14]:

$$\frac{\Delta\sigma}{\sigma_d} = \frac{1}{\mu}\frac{\partial\mu}{\partial T_e}\bigg|_{T_e=T} \Delta T, \tag{7}$$

where T is the lattice temperatures, $\Delta T = T_e - T$, and σ_d is the conductivity without irradiation. We readily see that the sign of the photoconductive signal is determined by that of the derivative $\partial\mu/\partial T_e$. In the case of predominant scattering by phonons, which is relevant to our experiment, the sign of the photoconductivity is negative [36]. In a biased structure, photoexcited change of sample resistance results in a dc current proportional to the second power of the radiation electric field E at frequency ω and the static field $\boldsymbol{E}(\omega = 0)$ [14]:

$$j_\alpha = \sigma^{(3)}_{\alpha\beta\gamma\delta} E_\beta(\omega) E^*_\gamma(\omega) E_\delta(\omega = 0), \tag{8}$$

with conductivity $\sigma^{(3)}_{\alpha\beta\gamma\delta} \equiv \sigma^{(3)}_{\alpha\beta\gamma\delta}(\omega, -\omega, 0)$. The dc current caused by the increase of QW resistance is detected in a circuit sketched in Fig. 2a as a voltage drop across load resistance. The response time of μ-photoconductivity is determined by fast times of free carrier energy relaxation, which depends on temperature lying in the ps to ns range. Thus, excitation by 100-ns pulses with ns time scale spikes caused by spontaneous mode-locking results in a fast photoconductive response, which repeats the temporal structure of the radiation pulse. More details on the mechanisms of THz photoconductivity can be found in e.g. Ref. [14].

Due to symmetry arguments, photoconductivity is the only optoelectronic effect, which can be excited in our large homogeneous (001)-oriented QWs (wafers of type #A) excited by THz radiation at normal incidence [14, 23]. In (110)-grown QWs (wafers of type #B), the symmetry of QW is reduced to C_{2v} point group, which makes possible generation of photogalvanic effects in unbiased samples even at normal incidence [37, 38]. This linear photogalvanic effect has been used in our work to provide additional evidence for the anomalous gold film penetrability applying an independent method. The LPGE arises in homogeneous samples under spatially homogeneous optical excitation. It is due to the "built-in" symmetry properties of the media interacting with the radiation field and is caused by an asymmetry in $\boldsymbol{k}$-space of the carrier photoexcitation and of the momentum relaxation due to scattering of free carriers on, e.g., phonons in noncentrosymmetric crystals (for reviews see [14, 23, 39, 40]). The linear photogalvanic current density $\boldsymbol{j}$ is phenomenologically described by the following expression [23]:

$$j_\lambda = \sum_{\mu,\nu} \chi_{\lambda\mu\nu} \frac{1}{2}(E_\mu E^*_\nu + E_\nu E^*_\mu) \tag{9}$$

linking the dc current to the symmetrized product $\{E_\mu E^*_\nu\}$ by a third-rank tensor $\chi_{\lambda\mu\nu}$, which is symmetric in the last two indices. The index λ enumerates two in-plane coordinates of QW x and y, while μ and ν run over all three Cartesian coordinates. Therefore, $\chi_{\lambda\mu\nu}$ is isomorphic to the piezoelectric tensor and may have

nonzero components in media lacking a center of symmetry. The linear photogalvanic effect represents a microscopic ratchet. The periodically alternating electric field superimposes a directed motion on the thermal velocity distribution of carriers in spite of the fact that the oscillating field does not exert a net force on the carriers or induce a potential gradient. The directed motion is due to nonsymmetric random relaxation and scattering in the potential of a noncentrosymmetric medium [41–43]. The polarization dependence of the LPGE current density j_x for normal incidence by linearly polarized radiation follows from Eq. 9 and is given by [37, 44, 45]:

$$j_x = (\chi_+ + \chi_- \cos 2\alpha)\, P\,, \tag{10}$$

where $\chi_\pm = (\chi_{xyy} \pm \chi_{xxx})/2$, x is parallel to the mirror reflection plane of QW, radiation power $P \propto E^2$, and E is the amplitude of the radiation electric field exciting 2DEG. The polarization dependence describes well our experimental data with fitting parameters $\chi_\pm$ (see solid lines in Fig. 8a and b for the illumination of gold-film-free and gold-film-covered parts of the sample #B). The response time of the LPGE is determined by the fast momentum relaxation time. Thus, also for the LPGE, current excitation by 100-ns pulses with ns time scale spikes caused by spontaneous mode-locking results in a fast response, which repeats the temporal structure of the radiation pulse (see Fig. 8). Microscopic details of the LPGE in GaAs QWs excited by THz radiation are well researched and described in e.g. [14, 23].

Appendix 3: Gold Film Fabrication and Characteristics

A. MBE Gold Film Growth

Samples #A1, #A2, and #A4 were made out of metal/semiconductor hybrid films grown completely in a MBE cluster. This means that after the semiconductor growth, the wafers were transferred in situ from a semiconductor chamber to dedicated metal chamber, where the Au layers were grown on parts of the 2-in. wafer using mobile shadow mask. The base pressure of the metal chamber is around 5×10^{-11} mbar. Reflection high-energy electron diffraction (RHEED) was used to check the crystalline quality of the layer, and to crosscheck the growth rate by RHEED oscillations (see Fig. 11). For gold, oscillations with 40 s/ML were obtained. The thickness of the grown layers was additionally controlled by a calibrated quartz microbalance. In Fig. 11c, the thin streaky RHEED pattern, here for 20 nm Au layer grown on wafer #A4, indicates the high crystalline quality of the Au layer grown at 200°C substrate temperature.

X-Ray photoemission spectroscopy (XPS) from 40-nm Au films revealed that the topmost layer consists of Au, O, C, Ga, and As. O and C are known to be present at all surfaces exposed to air. Ga and As are also known to be present in the topmost layer [46, 47] after growth of Au directly on GaAs. In the initial growth stage, the Au atoms seem to get completely incorporated into the very first Ga and As layers, where a phase separation into Au-Ga phases may take place, triggered by the impinging Au atoms. After growth of a few nanometers, a pure Au layer is formed between the

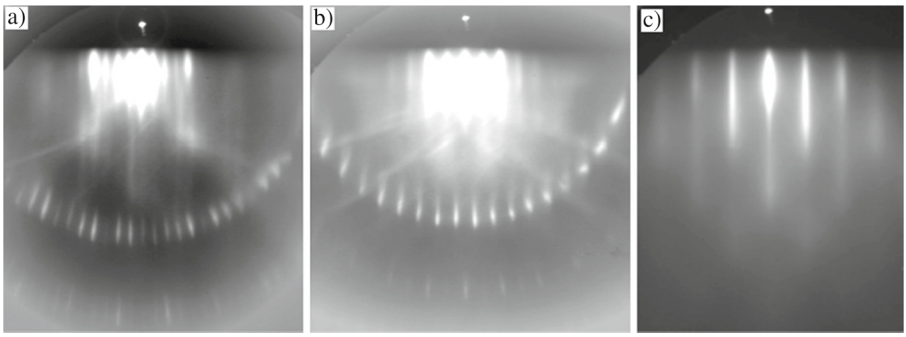

Fig. 11 RHEED images for **a** GaAs(001) along the (100), **b** along the (011) direction, and **c** for 20 nm Au grown on GaAs(001)

thin surface layer containing Au, Ga, and As and the underlying semiconductor heterostructure [46–48]. By Ar ion bombardment at 1000 eV for 15 min, which removes approximately 3–6 nm from the top, the XP spectra show a pure Au layer without any contaminants, which means that the Ga and As contamination is not present throughout the whole Au layer. Hence, this result confirms a floating Ga-Au-As layer on top of a pure Au film.

B. Electric Characteristic of Gold Films

Electric characteristics of gold were obtained by measuring resistivity of MBE-grown 20-nm film. The resistivity was determined applying van-der-Pauw method [49]. For that, we used samples with square-shaped 2×2 mm^2 gold films of 20 nm thickness. Four contacts to the film were fabricated with silver-conducting varnish. Using the fact that in our samples the distance between contacts is substantially larger than the film thickness, we calculated the specific resistivity after [49]:

$$\rho = \frac{\pi d}{ln2} \frac{R_{12,34} + R_{23,41}}{2} F \tag{11}$$

here d is the film thickness (20 nm), $R_{12,34} = V_{34}/I_{12}$ and $R_{23,41} = V_{41}/I_{23}$ are resistances, V_{34}, V_{41}, I_{12}, and I_{23} are voltages and currents measured from the corresponding contacts, and factor $F = 1$, because in our measurements $R_{12,34} \approx R_{23,41}$.

Room temperature resistivity of various films obtained by this method are given in Table 1 together with the values of applied currents, measured signals, and calculated resistances for different pairs of contacts. The obtained values, being of the order of $4.6 - 5.8 \cdot 10^{-8}\ \Omega \cdot$ m, are close to that obtained in Ref. [17] for 85-nm-thick film ($8.7 \cdot 10^{-8}\ \Omega \cdot$ m). Both values are several times larger than the value of the bulk gold resistivity $2.25 \cdot 10^{-8}\ \Omega \cdot$ m (see, e.g. [50]). Note that the increase of specific resistivity with the film thickness decrease is well known (see e.g. [16]). Using the specific resistivity from Table 1, we obtain for room temperature and $f = 2.54$ THz the skin depth $\delta_s \approx 65$ nm.The decrease of temperature results in a decrease of the specific resistivity and, consequently, of the skin depth.

Table 1 Specific resistivity ρ of 20 nm Au films measured by van-der-Pauw method

Sample		Current (μA)	$U_{12,34}$ (μV)	$U_{23,41}$ (μV)	$R_{12,34}$ (Ω)	$R_{23,41}$ (Ω)	ρ ($\Omega \cdot m$)
#A3-20M	MBE	10	5.07	5.03	0.507	0.503	$4.6 \cdot 10^{-8}$
#A4-20M	MBE	10	5.52	4.94	0.552	0.494	$4.8 \cdot 10^{-8}$
#B-20E	Evaporated	10	6.52	6.14	0.652	0.614	$5.8 \cdot 10^{-8}$

Current, voltages, and resistances are values with that the surface resistance was obtained. Measurements applying lower current yielded the same result

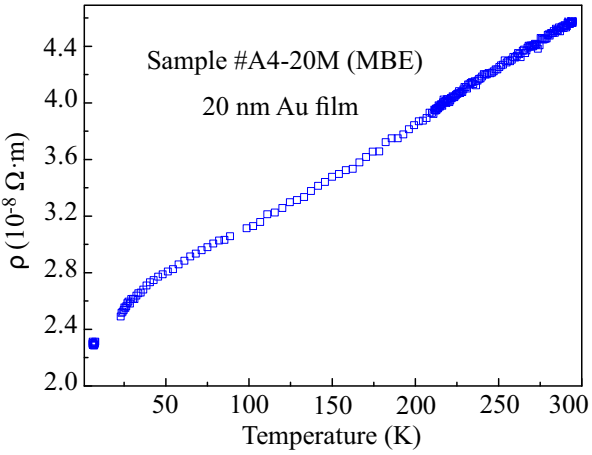

Fig. 12 Temperature dependence of the specific resistivity ρ measured on a MBE-grown 20-nm gold film

Temperature dependence of the gold film specific resistivity is shown in Fig. 12. The data were obtained applying 10 μA (ac) current with frequency 12 Hz. The corresponding voltage drop was measured by lock-in amplifier SR830.

Acknowledgments We thank L. E. Golub for fruitful discussions.

Funding Open Access funding enabled and organized by Projekt DEAL. Financial support was received from the Deutsche Forschungsgemeinschaft (DFG, German Research Foundation) - Project-ID 314695032 - SFB 1277, the Volkswagen Stiftung Program (97738), and the IRAP programme of the Foundation for Polish Science (grant MAB/2018/9, project CENTERA).

References

1. D. W. Lynch and W. R. Hunter, *Comments on the Optical Constants of Metals*, in: *Handbook of Optical Constants of Solids*, Ed. E. D. Palik, Vol.1, p. 275, Acad. Press (1998).
2. J. E. Sipe and G.I. Stegeman, *Nonlinear Optical Response of Metal Surfaces,* Ch. 15 in *Surface Polaritons*, ed. by V. M. Agranovich and D. L. Mills, Modern Problems in Condensed Matter Sciences Vol. 1 (North Holland, Amsterdam, 1983).
3. M. A. Paesler and P. J. Moyer, *Near-Field Optics: Theory, Instrumentation, and Applications* (Wiley-Interscience, 1996). ISBN-10: 0471043117 ISBN-13: 978-0471043119.
4. D. Courjon, *Near-field Microscopy And Near-field Optics* (Imperial College Press, 2003). ISBN-10: 186094258X ISBN-13: 978-1860942587.
5. M. Ohtsu, *Progress in Nano-Electro-Optics I: Basics and Theory of Near-Field Optics*, Springer Series in Optical Sciences, Band 86, (Springer, Berlin, Heidelberg, 2010). ISBN-10: 364207801X ISBN-13: 978-3642078019.
6. *Near-Field Optics and Surface Plasmon Polaritons Nanostructured gold films as broadband terahertz antireflection coatings*, Topics in Applied Physics, Band 81, Ed. S. Kawata (Springer, Berlin, Heidelberg, 2010). ISBN-10: 3642074766 ISBN-13: 978-3642074769.
7. L. Novotny and B. Hecht, *Principles of Nano-Optics* (Cambridge University Press, 2012). ISBN-10: 1107005469 ISBN-13: 978-1107005464.
8. O. Keller, *Quantum Theory of Near-Field Electrodynamics (Nano-Optics and Nanophotonics)* (Springer, 2012). ISBN-10: 3642174094 ISBN-13: 978-3642174094.
9. N. Talebi, *Near-Field-Mediated Photon-Electron Interactions*, Springer Series in Optical Sciences, Band 228 (Springer, 2019). ISBN-10: 3030338150 ISBN-13: 978-3030338152.
10. M. Moskovits, *Surface-enhanced spectroscopy*, Rev. Mod. Phys. 57, 783 (1985).
11. *Surface Enhanced Raman Scattering: Physics and Applications*, Eds.: K. Kneipp, M. Moskovits, and H. Kneipp (Springer, 2006).
12. S. D. Ganichev, A. Ya. Shul'man, I. N. Kotel'nikov, N. A. Mordovets, and W. Prettl, *Response of tunnel Schottky-barrier junction to radiationpressure of FIR radiation*, Int. J. of Infrared and Millimeter Waves **17**, 1353 (1996).
13. A. Ya. Shulman, *Edge condition in diffraction theory and maximum enhancement of electromagnetic field in the near zone*, physica status solidi (a) 175, 279 (1999).
14. S. Ganichev and W. Prettl, *Intense Terahertz Excitation of Semiconductors* (Oxford University Press, 2006).
15. P. Olbrich, J. Kamann, M. König, J. Munzert, L. Tutsch, J. Eroms, D. Weiss, Ming-Hao Liu, L. E. Golub, E. L. Ivchenko, V. V. Popov, D. V. Fateev, K. V. Mashinsky, F. Fromm, Th. Seyller, and S. D. Ganichev, *Terahertz ratchet effects in graphene with a lateral superlattice*, Phys. Rev. B **93**, 075422 (2016).
16. M. Walther, D. G. Cooke, C. Sherstan, M. Hajar, M. R. Freeman, and F. A. Hegmann, *Terahertz conductivity of thin gold films at the metal-insulator percolation transition*, Phys. Rev. **B 76**, 125408 (2007).
17. N. Laman and D. Grischkowsky, *Terahertz conductivity of thin metal films*, Appl. Phys. Lett. **93**, 051105 (2008).
18. N. C. Lindquist, P. Nagpal, K. M. McPeak, D. J. Norris, and S. H. Oh, *Engineering metallic nanostructures for plasmonics and nanophotonics*, Rep. Prog. Phys. **75**, 036501 (2012).
19. J. Lloyd-Hughes and T.-I. Jeon, *A Review of the Terahertz Conductivity of Bulk and Nano-Materials,* JIRMMTeraWav. **33**, 871 (2012).
20. M. Tinkham, *Energy Gap Interpretation of Experiments on Infrared Transmission through Superconducting Films*, Phys. Rev. **104**, 845 (1956).
21. J. J. Tu, C. C. Homes, and M. Strongin, Phys. Rev. Lett **90**, 017402 (2003).
22. A. E. Kaplan, *Metallic nanolayers: a sub-visible wonderland of optical properties*, J. Opt. Soc. of America B **35**, 328 (2018).
23. E. L. Ivchenko, *Optical Spectroscopy of Semiconductor Nanostructures* (Alpha Science, Harrow UK, 2005).
24. Z. D. Kvon, S. N. Danilov, D. A. Kozlov, C. Zoth, N. N. Mikhailov, S. A. Dvoretskii, and S. D. Ganichev, *Cyclotron Resonance of Dirac Ferions in HgTe Quantum Wells*, JETP Lett. **94**, 816 (2011).
25. P. Olbrich, C. Zoth, P. Vierling, K.-M. Dantscher, G. V. Budkin, S. A. Tarasenko, V. V. Bel'kov, D. A. Kozlov, Z. D. Kvon, N. N. Mikhailov, S. A. Dvoretsky, and S. D. Ganichev, *Giant photocurrents in a Dirac fermion system at cyclotron resonance*, Phys. Rev. B **87**, 235439 (2013).
26. Note that in (001)-grown QWs structures #A1, #A2, #A3 and #A4 photogalvanic effects at normal incidence are forbidden by symmetry arguments.

27. M. Born and E. Wolf, *Principles of Optics: Electromagnetic Theory of Propagation, Interference and Diffraction of Light* (Cambridge University Press, 1999).
28. R. L. Olmon, B. Slovick, T. W. Johnson, D. Shelton, S.-H. Oh, G. D. Boreman, and M. B. Raschke, *Optical dielectric function of gold*, Phys. Rev. B **86**, 235147 (2012).
29. M. A. Ordal, L. L. Long, R. J. Bell, S. E. Bell, R. R. Bell, R. W. Alexander, and C. A. Ward, *Optical properties of the metals Al, Co, Cu, Au, Fe, Pb, Ni, Pd, Pt, Ag, Ti, and W in the infrared and far infrared*, Appl. Opt. **22**, 1099 (1983).
30. S. D. Ganichev, *Tunnel ionization of deep impurities in semiconductors induced by terahertz electric fields*, Physica B **273-274**, 737 (1999).
31. S. D. Ganichev, E. Ziemann, Th. Gleim, W. Prettl, I. N. Yassievich, V. I. Perel, I. Wilke, and E. E. Haller, *Carrier tunneling in high-frequency electric fields*, Phys. Rev. Lett. **80**, 2409 (1998).
32. S. D. Ganichev, S. N. Danilov, V. V. Bel'kov, E. L. Ivchenko, M. Bichler, W. Wegscheider, D. Weiss, and W. Prettl, *Spin sensitive bleaching and monopolar spin orientation in quantum wells*, Phys. Rev. Lett. **88**, 057401-1 (2002).
33. S. D. Ganichev, Petra Schneider, V. V. Bel'kov, E. L. Ivchenko, S. A. Tarasenko, W. Wegscheider, D. Weiss, D. Schuh, B. N. Murdin, P. J. Phillips, C. R. Pidgeon, D. G. Clarke, M. Merrick, P. Murzyn, E. V. Beregulin, and W. Prettl, *Spin galvanic effect due to optical spin orientation,* Phys. Rev. B. (Rapid Communic.) **68**, 081302 (2003).
34. S. D. Ganichev, S. N. Danilov, V. V. Bel'kov, S. Giglberger, S. A. Tarasenko, E. L. Ivchenko, D. Weiss, W. Jantsch, F. Schäffler, D. Gruber, and W. Prettl, *Pure spin currents induced by spin-dependent scattering processesin SiGe quantum well structures*, Phys. Rev. B **75**, 155317 (2007).
35. S. D. Ganichev, Ya. V. Terent'ev, and I. D. Yaroshetskii, *Photon-drag photodetectors for the far-IR and submillimeter regions*, Sov. Tech. Phys. Lett. **11**, 20 (1985).
36. K. Seeger, *Semiconductor Physics* (Springer, Wien, 1997).
37. V. A. Shalygin, H. Diehl, Ch. Hoffmann, S. N. Danilov, T. Herrle, S. A. Tarasenko, D. Schuh, Ch. Gerl, W. Wegscheider, W. Prettl, and S.D. Ganichev, *Spin photocurrents and circular photon drag effect in (110)-grown structures*, JETP Lett. **84**, 570 (2006).
38. S. D. Ganichev and L. E. Golub, *Interplay of Rashba/Dresselhaus spin splittings probed by photogalvanic spectroscopy*, phys. stat. solidi b - basic solid state physics **251**, 1801, (2014).
39. B. Sturman and V. Fridkin, *The photovoltaic and photorefractive effects in non-centrosymmetric materials* (Gordon & Breach, Philadelphia, 1992).
40. E. L. Ivchenko and G. E. Pikus. *Superlattices and other heterostructures* (Springer, 1997).
41. P. Hänggi and F. Marchesoni, *Artificial Brownian motors: Controlling transport on the nanoscale*, Rev. Mod. Phys. **81**, 387 (2009).
42. W. Weber, L. E. Golub, S. N. Danilov, J. Karch, C. Reitmaier, B. Wittmann, V. V. Bel'kov, E. L. Ivchenko, Z. D. Kvon, N. Q. Vinh A. F. G. van der Meer, B. Murdin, and S. D. Ganichev, *Quantum ratchet effects induced by terahertz radiation in GaN-based two-dimensional structures*, Phys. Rev. B **77**, 245304 (2008).
43. E. L. Ivchenko and S. D. Ganichev, *Ratchet effects in quantum wells with a lateral superlattice*, JETP Lett. **93**, 673-682 (2011).
44. H. Diehl, V. A. Shalygin, V. V. Bel'kov, Ch. Hoffmann, S. N. Danilov, T. Herrle, S. A. Tarasenko, D. Schuh, Ch. Gerl, W. Wegscheider, W. Prettl, and S. D. Ganichev, *Spin photocurrents in (110)-grown quantum well structures* New J. Physics **9**,*Focus on Spintronics in Reduced Dimensions*, 349 (2007).
45. V. V. Bel'kov, S. D. Ganichev, Petra Schneider, C. Back, M. Oestreich, J. Rudolph, D. Hägele, L. E. Golub, W. Wegscheider, and W. Prettl, *Circular Photogalvanic Effect at Inter-Band Excitation in Semiconductor Quantum Wells*, Solid State Communic. **128**, 283 (2003).
46. T. G. Andersson, *The initial growth of vapour deposited gold films*, Gold Bull. **15**, 7-18 (1982).
47. A. Hiraki, S. Kim, W. Kammura, and M. Iwami, *Dynamical observation of room temperature interfacial reaction in metal-semiconductor system by Auger electron spectroscopy*, Surface Science **86**, 706 (1979).
48. C. S. Patuwathavithane, J. R. Williams, C. C. Tin, P. A. Barnes, and M. J. Bozack, *An RBS analysis of the low temperature mass transport of Au in GaAs*, Nucl. Inst. Methods Phys. Res. B **56-57**, 753 (1991).
49. L. J. van der Pauw, *A method of measuring the resistivity and Hall coefficient onlamellae of arbitrary shape*. Philips Techn. Rev. **20**, 220 (1958).
50. *Handbook of Optical Constants of Solids*, E. D. Palik (ed.) (Acad. Press, N.-Y., 1998).